INTERNATIONAL JOURNAL FOR NUMERICAL METHODS IN FLUIDS
Int. J. Numer. Meth. Fluids 2006; **51**:1355–1377
Published online 10 February 2006 in Wiley InterScience (www.interscience.wiley.com). DOI: 10.1002/fld.1164

Numerical analysis of a 3D hydrodynamic contact

Costin Alin Caciu*,† and Etienne Decencière‡

CMM, École des Mines de Paris, 35, rue Saint-Honoré, 77305 Fontainebleau, France

SUMMARY

We study here the numerical analysis of a hydrodynamic contact in a particular configuration: the 3D incompressible viscous flow of a fluid dragged by a smooth plate over a rough surface. The mathematical model takes into account and discretizes the local topography of the rough profile. The simulation outcome will be the 3D velocity and pressure fields of the fluid film within the contact borders. This work is limited to the study of numerical resolution methods working solely in finite differences. The algorithms will be tested by analysing and comparing their results with analytically known flows.

KEY WORDS: friction; hydrodynamic lubrication; incompressible flow; Navier–Stokes equations; CFD

1. INTRODUCTION

Energy loss and friction phenomena have always been domains of major interest for the scientists. In this context, the present work tries to characterize, numerically, the tribological properties of rough surfaces in a particular configuration: the 3D incompressible viscous flow in the hydrodynamic contact between a smooth plate and a rough surface. The geometry of the contact is strongly related to the physical parameters of the flow. Generally, in such conditions, the fluid film is relatively thin but always thicker than the surface roughness characteristic size, so that no elastic contact occurs.

This study is performed within the framework of a friction prediction tool for hydrodynamic contacts. First, this tool will enable us to analyse in depth the flows in hydrodynamic bearings and to obtain significant results concerning the influence of the surface topography on the contact tribological performance. Furthermore, the tool may be used, as objective function, to perform topography optimization for friction reduction issues.

*Correspondence to: Costin Alin Caciu, CMM, École des Mines de Paris, 35, rue Saint-Honoré, 77305 Fontainebleau, France.
†E-mail: Costin.Caciu@cmm.ensmp.fr
‡E-mail: Etienne.Decenciere@cmm.ensmp.fr

Received 4 July 2005
Revised 7 November 2005
Accepted 7 November 2005

The surfaces studied are available as 2D topographic images. Image processing tools have been developed in order to extract and analyse the topographic characteristics of such rough surfaces [1]. Nevertheless, their application is limited; the physical phenomena occurring in the hydrodynamic contact are complex, and global parameters like drag or lift are difficult to estimate from the topographic analysis of the surface alone.

Consequently, we propose a 3D hydrodynamic contact model; the inputs will be the rough surface as a 2D image and the physical and geometrical parameters; the fluid flow in the defined volume will be examined. Despite the wish to build as generic a model as possible, several assumptions have to be introduced in order to simplify our study.

2. THE PHYSICAL MODEL

We consider a viscous incompressible fluid, at time t, inside a volume limited on the upper side by a smooth plate $\mathscr{P}$ and on the lower side by a rough surface $\mathscr{R}$. We obtain a bounded domain of $\mathbb{R}^3$, that we denote Ω (Figure 1). In the direct orthogonal reference $(0, \boldsymbol{i}_1, \boldsymbol{i}_2, \boldsymbol{i}_3)$, attached to a terrestrial reference, Ω is defined as follows:

$$\forall x \in \mathbb{R}^3,\ x = (x_1, x_2, x_3) \ \in \ \Omega \iff \begin{cases} 0 \leqslant x_1 \leqslant l_1 \\ 0 \leqslant x_2 \leqslant l_2 \\ f(x_1, x_2) \leqslant x_3 \leqslant l_3 \end{cases} \tag{1}$$

f being the function describing the rough surface $\mathscr{R}$. Ω dimensions are l_1, l_2 and l_3 and we denote $\partial\Omega$ the sub-domain containing the borders of Ω. We suppose $f(x_1, x_2) < l_3$ for all (x_1, x_2) such that $0 \leqslant x_1 \leqslant l_1$ and $0 \leqslant x_2 \leqslant l_2$.

The rough surface $\mathscr{R}$ is motionless and the smooth plate $\mathscr{P}$ moves with the velocity $\boldsymbol{v}_p = (v_p, 0, 0)$. The movement of the fluid generated by the displacement of the smooth plate $\mathscr{P}$ is defined by its velocity $\boldsymbol{v} = (v_1, v_2, v_3)(x, t)$ and by its pressure $p = p(x, t)$. The downstream and upstream pressures are settled to $p(l_1, x_2, x_3) = p_1$ and $p(0, x_2, x_3) = p_2$.

Assumptions

The mathematical description of the previous flow is associated to a set of physical assumptions which constitute the *physical model* [2–4]. The numerical results will permit,

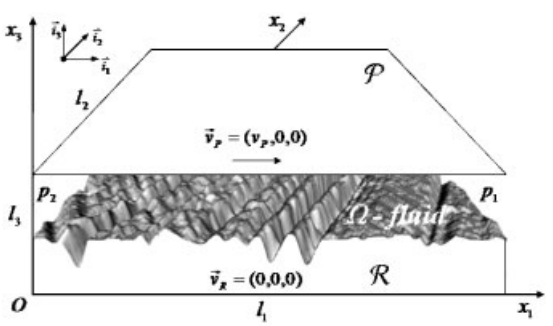

Figure 1. 3D contact.

a posteriori, to reject or to accept these assumptions, limiting the universality of the model. The mathematical formulation is based on the following presumptions:

- c_1. The fluid is considered Newtonian and incompressible, i.e. the velocity is supposed to be small compared to the sound velocity and wave phenomena are neglected.
- c_2. Thermodynamics do not play any role, the physical parameters of the fluid (density ρ, viscosity $\mu, \ldots$) are considered constant. The only unknown variables are the velocity vector $\boldsymbol{v}$ and the pressure field p.
- c_3. Any chemical reaction is excluded in the monophasic presumed fluid.
- c_4. The fluid adheres totally to solids (no-slip boundaries).
- c_5. Remote forces (gravity) are neglected.

Any information on Ω' external geometry is unknown. We want to obtain the velocity and pressure fields of the fluid dragged by $\mathscr{P}$, that we consider infinite, over $\mathscr{R}$, in steady-state conditions. This implies that the mentioned fields are constant in the chosen reference, the one attached to $\mathscr{R}$ and the study is then stationary.

2.1. Reynolds equation

In most of the tribology literature, hydrodynamic contact issues are generally solved using a classical or modified Reynolds equation, which is a simplification of the full Navier–Stokes equations. Examples of such applications are available in References [5, 6]. This equation requires two additional assumptions, altogether with those established in Section 2:

- c_6. The pressure is constant through the fluid film (no pressure variation along x_3-axis).
- c_7. The flow is laminar (no turbulence).

The two-dimensional steady-state Reynolds equation for the incompressible laminar flow involved in the hydrodynamic contact described by our model (Figure 2) is given by

$$\frac{\partial}{\partial x_1}\left(h^3\frac{\partial p}{\partial x_1}\right)+\frac{\partial}{\partial x_2}\left(h^3\frac{\partial p}{\partial x_2}\right)=6\mu v_p\frac{\partial h}{\partial x_1} \tag{2}$$

Using Reynolds equation for configurations accepting the assumptions above is interesting mainly for two reasons. First, the equation is easier to solve than the full Navier–Stokes equations and its numerical implementation is considerably less onerous. Second, it is

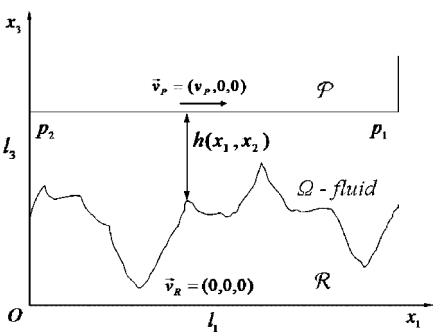

Figure 2. 2D contact.

commonly used for tribological issues and for numerous other studies similar to ours. Hence, referenced solutions are available to validate some of our results.

Nevertheless, this resolution approach is restrictive and brings consequent simplifications to the model. The applicability of Reynolds equation is limited to thin contact configurations (c_6 valid) for which the rough surface $\mathscr{R}$ infers laminar or laminar-approximate flows (c_7 verified). Therefore, Navier–Stokes equations will be employed in our case for further research. Besides the ability to study larger areas of rough topographies, this provides us with a more complete tool to explore the inner complex phenomena involved in hydrodynamic contacts and to analyse the influence of the topography on the tribological properties of rough surfaces.

2.2. Navier–Stokes equations

The general equations governing our physical model are those of Navier–Stokes, stationary and incompressible. In the velocity–pressure (primitive variables) formulation [2, 7], the momentum and continuity equations are

$$(\boldsymbol{v}\cdot\nabla)\boldsymbol{v}+\frac{1}{\rho}\nabla p-\nu\Delta\boldsymbol{v}=\boldsymbol{0} \tag{3}$$

$$\nabla\cdot\boldsymbol{v}=0 \tag{4}$$

ρ being the fluid density and ν the kinematic viscosity.

Moreover, in order to simplify the discretization and the numerical resolution, it is suitable to write the precedent equations in the non-dimensional formulation [8]. Therefore, we define a characteristic length $L=\min(l_1,l_2,l_3)$. The non-dimensional variables are

$$y=\frac{x}{L},\quad \boldsymbol{u}=\frac{\boldsymbol{v}}{v_p},\quad q=\frac{p}{\rho {v_p}^2} \tag{5}$$

One can notice that the dragging velocity v_p is brought to unity. In these variables, the non-dimensional Navier–Stokes equations become:

$$(\boldsymbol{u}\cdot\nabla)\boldsymbol{u}+\nabla q-\frac{1}{Re}\triangle\boldsymbol{u}=\boldsymbol{0} \tag{6}$$

$$\nabla\cdot\boldsymbol{u}=0 \tag{7}$$

The system parameters gather into only one non-dimensional parameter, the Reynolds number:

$$Re=\frac{v_pL}{\nu} \tag{8}$$

which is the ratio between the momentum convection (non-linear) and the momentum diffusion (linear), or between the inertial and the friction forces. The Reynolds number varies linearly with v_p and for considerable velocities the flow may be non-laminar. Therefore, neither the momentum convection nor the momentum diffusion will be neglected.

Working at real scale, with significant Reynolds numbers and in presence of the roughness of $\mathscr{R}$ leads to a complex model, as no additional simplification to the preceding equations is possible. On the other hand, the Reynolds numbers we work with are of the same order as those of real configurations, which is essential for the relevance of the simulation results.

2.3. Boundary conditions

To solve Reynolds or Navier–Stokes equations, boundary conditions have to be added. Considering a total adhesion of the fluid to solid surfaces, conventional no-slip wall boundary conditions (no-slip velocity and zero pressure gradient) are required on plate $\mathscr{P}$:

$$\boldsymbol{v}|_{(x\in\mathscr{P})} = v_p \cdot \boldsymbol{i}_1 \tag{9}$$

$$\left.\frac{\partial p}{\partial \mathbf{n}}\right|_{(x\in\mathscr{P})} = 0 \tag{10}$$

and on the rough surface $\mathscr{R}$:

$$\boldsymbol{v}|_{(x\in\mathscr{R})} = \mathbf{0} \tag{11}$$

$$\left.\frac{\partial p}{\partial \mathbf{n}}\right|_{(x\in\mathscr{R})} = 0 \tag{12}$$

$\mathbf{n}$ being the normal to the solid surface in each point x. In addition, these conditions are completed by the imposed upwind and downwind pressures:

$$p(l_1, x_2, x_3) = p_1, \quad p(0, x_2, x_3) = p_2 \tag{13}$$

It should be noticed that the boundary conditions are incomplete; there is no condition on x_2-axis. As no additional information is available, several options are feasible.

The first would be to impose *restrictive* Dirichlet conditions, alternative that requires prior assumptions on the flow inside the contact.

A second option, widely used in applications, is to use *periodic* boundary conditions though they are not suited to our problem; indeed, the borders corresponding to $x_2 = 0$ and l_2 may be very dissimilar and periodicity would induce discontinuities and inconsistency in the continuity equation.

A third option, as a solution to the discontinuities produced by the periodic boundaries, would be to extend the computation domain by adding a mirror of $\mathscr{R}$ starting from $x_2 = l_2$, as illustrated in Figure 3, and to apply *periodic* boundary conditions to the new domain. Beside the duplication of the computation domain as a result of the mirror operation, another impediment brought by this solution consists in the spurious values resulting for $x_2 = 0$ and l_2.

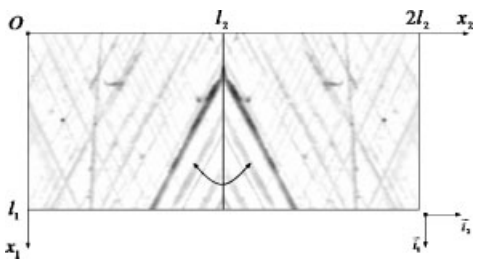

Figure 3. Mirror–boundary conditions.

Finally, another option would be that the boundary values be required to satisfy an extrapolation condition (consistent with the continuity equation); specifically, they must satisfy *free-boundary*-type conditions:

$$\frac{\partial \boldsymbol{v}}{\partial x_2}(x_1, 0, x_3) = \mathbf{0}, \quad \frac{\partial \boldsymbol{v}}{\partial x_2}(x_1, l_2, x_3) = \mathbf{0} \tag{14}$$

According to the resolution method used, *restrictive* or *free* boundary conditions will be further employed.

2.4. Cavitation conditions

A notable phenomenon that may occur in a hydrodynamic contact, under specific conditions, is fluid cavitation. It consists in the formation of gas cavities in the diverging regions of the fluid film, which has a strong influence on the hydrodynamic pressure. This consequently has an effect on the flow inside the contact. Therefore the nature of the cavitations and the conditions under which these phenomena occur deserve a deeper examination.

Hamilton *et al*. [9] showed experimentally the presence of gas cavitations in micro-textured seal contacts, while Priest *et al.* [10] presented a detailed review of the physical nature of cavitation and alternative analytical models of film rupture and reformation. We employ here the commonly used *Reynolds* or *Swift–Steiber* continuity boundary conditions, which implies that, on the cavitation–fluid interface, the pressure gradient with respect to the direction normal to the boundary is zero:

$$p = p_{\text{cavity}}, \quad \frac{\partial p}{\partial x} = 0 \tag{15}$$

where the pressure in the gas cavities, p_{cavity}, is the saturation pressure of the dissolved gas which is generally assumed to be equal to the atmospheric pressure.

3. NUMERICAL RESOLUTION METHODS

We will devote this work to the resolution of the Navier–Stokes equations presented in Section 2.2, with no additional simplifications, by direct numerical simulation (DNS). This approach is the most accurate for turbulence reproduction and yields detailed information about the flow.

We have to solve the PDE system (3) and (4) which is of second order and non-linear. The unknown variables are the velocity and pressure fields $(\boldsymbol{v}, p)$.

Finite differences, *finite elements* or *spectral* methods may be employed for the numerical resolution of the PDE. Here, in the presence of roughness, we will restrict our choice to the *finite difference* approximation methods.

3.1. Numerical scheme

3.1.1. Discretization. For the discretization of the domain, several types of grids are available [11, 12]: *uniform orthogonal*, *non-uniform orthogonal* or *unstructured*. We choose to work with uniform orthogonal grids which have the simplest implementation. According to the

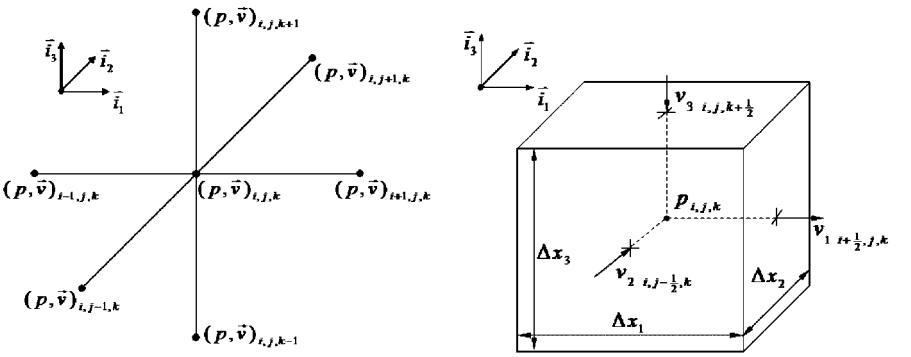

Figure 4. Uniform orthogonal grids: (a) Collocated grid; and (b) MAC (Marker and Cell) grid.

resolution method used, the grid employed may be *collocated* (Figure 4(a)) or *staggered* (Figure 4(b)).

Let $\triangle x_1$, $\triangle x_2$ and $\triangle x_3$ be the sampling steps used to sample the 3D domain. The discretization of the unknown variables $(\boldsymbol{v}, p)$ conduces to a 3D matrix of size $n_1 \times n_2 \times n_3$ with:

$$n_1 = \frac{l_1}{\triangle x_1} + 1, \quad n_2 = \frac{l_2}{\triangle x_2} + 1, \quad n_3 = \frac{l_3}{\triangle x_3} + 1$$

An important aspect to be examined is the isotropy of the grid spacing. Stability problems may occur if there are considerable dissimilarities between the different sampling steps. It results directly from the numerical implementation of the methods: the discrepancies between the different sampling steps may induce data overflows and can turn the algorithms unstable.

A valid simulation must also capture all of the kinetic energy dissipation. This occurs on the smallest scales, the ones on which viscosity is active, so the size of the grid spacing must not be greater than the determined *Kolmogorov* micro-scale:

$$\eta = \left(\frac{v^3}{\varepsilon}\right)^{1/4} \tag{16}$$

ε being the turbulence dissipation rate (into heat). It can be shown [12] that $\varepsilon \sim v_p^3/L$ and using (8) we deduce a practical expression for η:

$$\eta \sim \left(\frac{v^3 L}{v_p^3}\right)^{1/4} \tag{17}$$

The space steps $\triangle x_1$, $\triangle x_2$ and $\triangle x_3$ must therefore be smaller than the scale given by the expression above.

3.1.2. Iterative methods. Owing to the complexity of the PDE system (3) and (4), the computation of the associated matrix would be laborious. Moreover, the computation field being three dimensional and of considerable size, the direct solution of the system is not an option. Consequently, iterative methods will be employed. For this we will consider the unknown

fields (velocity and pressure in every point of the grid) as being a set of vectors $(\mathbf{v}^n, \mathbf{p}^n)$, defined by an initial state $(\mathbf{v}^0, \mathbf{p}^0)$ and an iterative law:

$$(\mathbf{v}^{n+1}, \mathbf{p}^{n+1}) = \Phi(\mathbf{v}^n, \mathbf{p}^n) \tag{18}$$

set which tends towards the system solution.

Another issue of Navier–Stokes equations is the non-linearity of the momentum equation (3). To apply iterative techniques and be able to write system (3) and (4) into the linear iterative formulation (18), it is necessary to linearize [13] the convection term $(\boldsymbol{v} \cdot \nabla)\boldsymbol{v}$. For this, we use the Euler formulation:

$$[(\boldsymbol{v} \cdot \nabla)\boldsymbol{v}]^{n+1} \simeq (\boldsymbol{v}^{n+1} \cdot \nabla)\boldsymbol{v}^n + (\boldsymbol{v}^n \cdot \nabla)\boldsymbol{v}^{n+1} - (\boldsymbol{v}^n \cdot \nabla)\boldsymbol{v}^n \tag{19}$$

There are several iterative methods working with finite differences. We will limit our study to the commonly used *relaxation* and *fractional-step* techniques. It is essential to explore several methods: first, being distinctive and using different discretization schemes, the comparison of their results allows to draw conclusions on their performance; second, by comparing their precision, convergence and robustness, we are able to choose the most suited ones to our issue.

3.2. Relaxation methods

The crucial point of the resolution algorithms for Navier–Stokes equations lies in the velocity–pressure coupling, which is the way to obtain the pressure update starting from the continuity and momentum equations. The relaxation techniques [12, 14] are iterative resolution methods which solve the *coupled* linear Navier–Stokes system, i.e. the velocity and the pressure are updated at the same time. Consequently, during computation, the momentum and continuity equations are satisfied simultaneously which implies that the conservative form may be used for the momentum equation.

Once the convective term linearization is done and the system discretization is performed, the global iterative linear system becomes:

$$\begin{pmatrix} \mathbf{v}^{n+1} \\ \mathbf{p}^{n+1} \end{pmatrix} = \mathbf{M} \cdot \begin{pmatrix} \mathbf{v}^n \\ \mathbf{p}^n \end{pmatrix} + \mathbf{N} \tag{20}$$

In our case, the iterative algorithm works locally, step by step, and does not employ the global form (20). This is mainly due to the complexity of the equations and the considerable size of the computation domain; indeed, the matrices $\mathbf{M}$ and $\mathbf{N}$ may be very large (up to $2^{24} \times 2^{24} = 2^{48}$ elements). The method stops when the computed values become steady.

Two relaxation techniques are available: *Jacobi* and *Gauss–Seidel*. In practice, the *Gauss–Seidel* technique is the most often used because it allows a faster convergence and uses less memory load. Classic *over* (or *under*)-*relaxation* techniques are also employed in order to accelerate (or decelerate, for robustness issues) the convergence rate.

3.2.1. Free-boundary conditions. The boundary conditions (9)–(13) are applied to the edges of the computation matrix. In addition, on x_2-axis, we use the free-boundary conditions (14) discussed in Section 2.4.

Unfortunately, the tests carried out with this implementation do not ensure the convergence of the system towards a stable solution. This lack of robustness is probably due to numerical issues related to the specificity of the computation domain. We work in a boundary layer zone in which the velocity variation terms are much higher than the pressure gradient terms. This may be a cause of the numerical instabilities encountered.

3.2.2. Restrictive boundary conditions. A different manner to apply boundary conditions and to avoid the free-boundary option in the current configuration is to replace the physical model by a different one, simplified with regard to the boundary conditions, and which will give similar results. It consists in adding to $\mathscr{R}$ smooth margins of dimensions proportional to its size (Figure 5). Thus, the rough profile $\mathscr{R}$ is framed by a smooth zone in which the flow study can be solved analytically. We neglect the effects of the inner turbulent flow on the edge flow (the margins are large enough) and vice versa; we suppose that the edges of the new field carry a planar Couette flow. In this case we can apply the relaxation algorithms with restrictive boundary conditions for all the borders of the new domain. For the planar Couette flow, in the current configuration, the Navier–Stokes equations are

$$\frac{\partial p}{\partial x_1} - \frac{1}{Re}\frac{\partial^2 v_1}{\partial x_3^2} = 0 \tag{21}$$

$$\frac{\partial p}{\partial x_2} = 0 \tag{22}$$

$$\frac{\partial p}{\partial x_3} = 0 \tag{23}$$

The pressure profile is thus linear $p(x_1) = ax_1 + b$ and the profile of the v_1 velocity component is parabolic $v_1(x_3) = c_1 x_3^2 + c_2 x_3 + c_3$. The boundary conditions (9)–(13) give the velocity and pressure fields expressions on the borders:

$$p(x_1, x_2, x_3)|_{\partial\Omega} = \frac{p_1 - p_2}{l_1} x_1 + p_2 \tag{24}$$

$$\begin{aligned} \boldsymbol{v}(x_1, x_2, x_3)|_{\partial\Omega} &= (v_1(x_3), 0, 0) \\ v_1(x_1, x_2, x_3)|_{\partial\Omega} &= \frac{Re}{2}\frac{p_1 - p_2}{l_1} x_3(x_3 - l_3) + \frac{v_p}{l_3} x_3 \end{aligned} \tag{25}$$

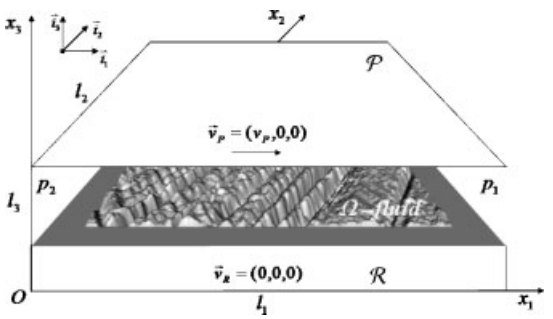

Figure 5. Restrictive boundary configuration.

The algorithm implemented with these new conditions has a faster convergence rate. The new boundary values are useful for the inner values update and their propagation inside the computation matrix is faster. Regarding the relevance and precision of the output results, the way in which the smooth margins are introduced plays an important part; indeed, it is necessary that their dimensions exceed a certain percentage (about 10–20%) of $\mathscr{R}$ dimensions so that the *non-interference* presumption remains valid. Moreover, the height level of these margins relative to the profile roughness mean level plays an important part; several positioning options are considered: *minimum*, *maximum*, *mean* or *median* value of $\mathscr{R}$ (Section 4.3).

3.2.3. Implementation. The selected relaxation algorithms work with the uniform orthogonal grid illustrated in Figure 4(a) which represents the computation volume by a 3D matrix. The two Jacobi and Gauss–Seidel techniques are implemented. The iterative methods are well adapted to this 3D study; if n is the characteristic size of the computation domain and n^3 the number of computation points it contains (in practice $n \sim 2^8$), there are about n^5 local elementary computations required for convergence while the direct methods (Gauss elimination) need about n^7. Moreover, the Gauss–Seidel Technique appears to be twice faster than the Jacobi one.

3.3. Fractional-step methods

Different methods have been devised in order to reduce the computational complexity of the original problem through a *separate* update of velocity and pressure fields. This strategy, called also fractional-step, is computationally very efficient compared with the coupled approach; however, the price for the decoupling may be some loss of accuracy.

The fractional step methods have been the subject of considerable discussion and improvement over the past years and nearly all numerical methods dedicated to solve Navier–Stokes equations in terms of primitive variables use this approach. There are several recent papers carrying interesting reviews and discussions on the fractional-step equations, the choice of intermediate boundary conditions and the accuracy of the methods [8, 12].

We will further examine and apply two of these approaches: the *projection* methods and the *artificial compressibility* methods, both introduced by Chorin in the late 1960s. In our application they will be implemented using MAC grids (Figure 4(b)).

3.3.1. Chorin–Temam projection scheme. The principle of projection methods is to advance the momentum equation and to enforce the continuity condition in separate steps. The theoretical framework is provided by the *Hodge* decomposition theorem, which states that any vector function $\tilde{\mathbf{v}}$ can be decomposed into a divergence-free part $\mathbf{v}$ plus the gradient of a scalar potential ϕ, i.e.

$$\tilde{\mathbf{v}} = \mathbf{v} + \nabla\phi \tag{26}$$

with $\nabla \cdot \mathbf{v} = 0$. In order to have a unique decomposition, boundary conditions must be specified as well. This class of schemes is now widely used in practice and has been rigorously analysed in References [15, 16].

The most classical projection method is the Chorin–Temam scheme. The typical form consists in three successive steps briefly described below:

1. Find a preliminary (intermediate) velocity $\tilde{\mathbf{v}}^{n+1}$ of the velocity field as the solution of the following semi-discrete problem:

$$\frac{1}{\triangle t}(\tilde{\mathbf{v}}^{n+1} - \mathbf{v}^n) + [(\tilde{\mathbf{v}} \cdot \nabla)\tilde{\mathbf{v}}]^{n+1} - \frac{1}{Re}\Delta\tilde{\mathbf{v}}^{n+1} = \mathbf{0} \quad \text{in } \Omega \tag{27}$$

$$\mathscr{B}(\tilde{\mathbf{v}}^{n+1}) = \mathbf{0} \tag{28}$$

   where $\mathscr{B}(\tilde{\mathbf{v}}^{n+1})$ represents a boundary condition for $\tilde{\mathbf{v}}^{n+1}$ which must be specified as a part of the method. The treatment of the non-linear term $[(\tilde{\mathbf{v}} \cdot \nabla)\tilde{\mathbf{v}}]^{n+1}$ may be performed using one of the linearization techniques presented in Section 3.1.2.
2. Determine $\mathbf{v}^{n+1}$ and p^{n+1} as being the solution of:

$$\begin{aligned} &\frac{1}{\triangle t}(\mathbf{v}^{n+1} - \tilde{\mathbf{v}}^{n+1}) + \nabla p^{n+1} = \mathbf{0} \quad \text{in } \Omega \\ &\nabla \cdot \mathbf{v}^{n+1} = 0 \end{aligned} \tag{29}$$

   with $\mathbf{v}^{n+1} \cdot \mathbf{n} = 0$ on $\partial\Omega$.

   This step can be reformulated in a way allowing the computation of $\mathbf{v}^{n+1}$ and p^{n+1} separately. Indeed, by formally applying the divergence operator on (29), we obtain the following Neumann problem for p^{n+1}:

$$\Delta p^{n+1} = \frac{1}{\triangle t}\nabla \cdot \tilde{\mathbf{v}}^{n+1} \quad \text{in } \Omega \tag{30}$$

$$\frac{\partial p^{n+1}}{\partial \mathbf{n}} = 0 \quad \text{on } \partial\Omega \tag{31}$$

   We have to notice that the Neumann condition on the pressure is a by-product of the projection and it may not be verified (in our case it is) by the original unsplit problem.
3. Finally, the end-of-step velocity field is obtained by updating $\mathbf{v}^{n+1}$ as follows:

$$\mathbf{v}^{n+1} = \tilde{\mathbf{v}}^{n+1} - \triangle t \nabla p^{n+1} \tag{32}$$

   using boundary conditions consistent with the previous ones.

On the basis of the above decomposition, the Chorin–Temam splitting is able to ensure the mass conservation of the solution (as the end-of-step velocity is divergence free). The chosen stop criterion is the small variation of the computed values between two successive iterations.

3.3.2. Implementation. The tests carried out with Artificial Compressibility algorithms show that these methods are not adapted to our boundary layer flow simulation. As for the Chorin–Temam projection scheme, its implementation proved to be stable, accurate and rather robust in terms of intermediate boundary conditions. Although its computational complexity is

reduced compared to the original problem, its convergence rate is slightly slower than the one shown by the relaxation techniques. In return, its major advantage comes from the decoupled update equations which allow pressure-correction cavitation conditions (Section 2.4) without perturbing the continuity equation.

3.4. Selected methods

The artificial-compressibility based algorithms being ineffective, the restrictive boundary relaxation (NS-r) and the projection (NS-p) methods have been selected for the simulation of non-laminar flows inside the hydrodynamic contact.

A relaxation algorithm for the resolution of Reynolds equations was also implemented (RE-r) in order to reduce the computational complexity when laminar flows occur in our hydrodynamic contact model.

The comparison and testing of the algorithms results will give a qualitative and quantitative measure of their precision, speed and applicability to the problem under study.

4. TESTS AND RESULTS

4.1. Context

The implementation of the computing methods has been performed within the framework of a hydrodynamic friction prediction tool. An overview of the global tool structure is illustrated in Figure 6. The model receives as input 2D images representing real or simulated (rough) surfaces, and the physical and geometrical parameters of the contact:

- Physical properties of the fluid: density ρ, viscosity μ.
- Boundary conditions: pressures p_1, p_2; velocity v_p.

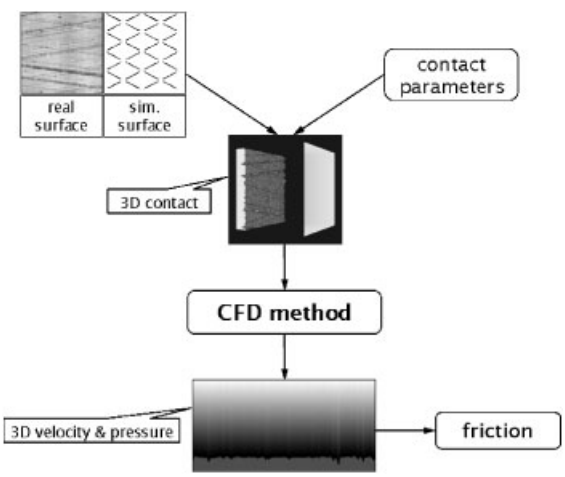

Figure 6. 3D prediction.

- Geometrical parameters of the contact: $\mathscr{R}'$ dimensions l_1, l_2, contact thickness l_3, grid spacing $\triangle x_1$, $\triangle x_2$, input image level scale $\triangle x_3$.

The output will consist in the velocity and pressure fields inside the contact. The initial conditions chosen for the velocity and pressure fields $(\mathbf{v}^0, \mathbf{p}^0)$ have a significant influence on the accuracy and the convergence rate of the algorithms; three choices are available:

- They are set to 0.
- They are set to average vales computed using the boundary values.
- They are set to approximate values corresponding to a planar Couette flow, easy to compute.

We will use the second option, which seems to be the best compromise in our case.

The algorithms were implemented in C++ using the `VTK©Kitware` library for data manipulation and the `Morphee©CMM-ENSMP` library for morphological image processing.

4.2. Physical measures

The detailed pressure and velocity fields give access to various local and global physical measures. A few of them are detailed below.

4.2.1. Viscous power loss. A way to verify the relevance of the results is to use the velocity and pressure fields to compute measurable physical quantities, that are characteristic of the contact. We can thus compare, through these quantitative measures, the results of the different algorithms implemented with experimental results. Starting from the velocity field and the fluid properties we can express the viscous dissipated power [2]:

$$P_{\text{viscous}} = \int_V \sum_{i,j} \left(\sigma_{ij} \frac{\partial v_i}{\partial x_j} \right) \mathrm{d}V = \frac{1}{2} \int_V \sum_{i,j} \left[\sigma_{ij} \left(\frac{\partial v_i}{\partial x_j} + \frac{\partial v_j}{\partial x_i} \right) \right] \mathrm{d}V \tag{33}$$

$\sigma_{i,j}$ being the *viscous constraint tensor* in an incompressible fluid:

$$\sigma_{ij} = \rho v \left(\frac{\partial v_i}{\partial x_j} + \frac{\partial v_j}{\partial x_i} \right) \tag{34}$$

We obtain finally the viscous power loss expression, in an incompressible fluid, that is dissipated irreversibly:

$$P_{\text{viscous}} = \frac{\rho v}{2} \int_V \sum_{i,j} \left(\frac{\partial v_i}{\partial x_j} + \frac{\partial v_j}{\partial x_i} \right)^2 \mathrm{d}V \tag{35}$$

which is in practice a measurable physical quantity. As we have local access to the velocity field we can also build easily the 3D friction losses field in the contact.

4.2.2. Flow. The fluid flow in the $\boldsymbol{i}_1$ and $\boldsymbol{i}_2$ directions can be easily computed, for each (x_1, x_2), by integrating the velocity over the appropriate surfaces, as illustrated in Figure 7.

The flow expressions are

$$Q_1(x_1) = \int_0^{l_3} \int_0^{l_2} u_1(x_1) \, \mathrm{d}x_2 \, \mathrm{d}x_3 \tag{36}$$

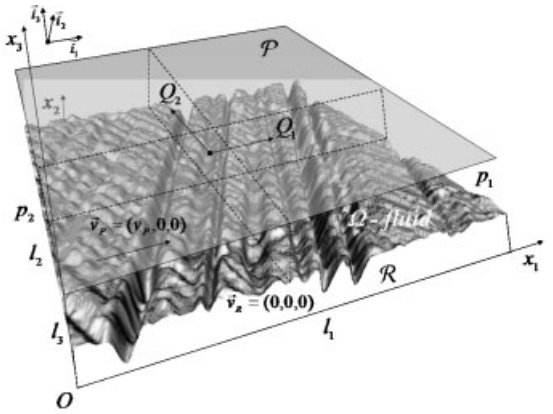

Figure 7. Average flow computation.

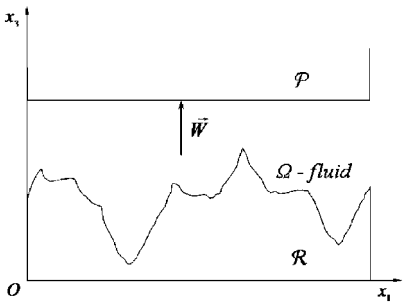

Figure 8. Load computation.

$$Q_2(x_2) = \int_0^{l_3} \int_0^{l_1} u_2(x_2)\, \mathrm{d}x_1\, \mathrm{d}x_3 \tag{37}$$

4.2.3. Load. If the pressure distribution is integrated over $\mathcal{P}$ area we obtain the total load that can be held by the fluid film (Figure 8).

The expression of the load is

$$W = \int_0^{l_2} \int_0^{l_1} p(l_3)\, \mathrm{d}x_1\, \mathrm{d}x_2 \tag{38}$$

4.3. Fluid film thickness

An important choice to make when building the 3D contact is the positioning of $\mathcal{P}$ relative to $\mathcal{R}$ (Figure 9).

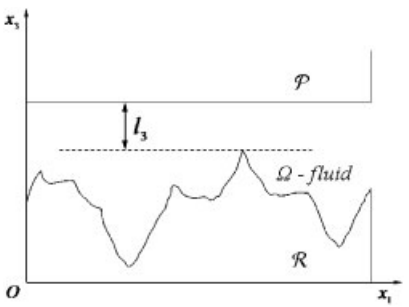

Figure 9. Contact thickness.

Several options are available:

- Starting from the minimum of $\mathscr{R}$.
- Starting from the maximum of $\mathscr{R}$.
- Starting from the average or the median value of $\mathscr{R}$.
- In order to contain a precise fluid quantity.
- *Dynamic*: if we consider an external force $\boldsymbol{F}_p$ on $\mathscr{P}$, the film thickness will be the result of the equilibrium between $\boldsymbol{F}_p$ and the force generated by the hydrodynamic load on $\mathscr{P}$.

This parameter is very important for the model as it considerably influences the results. However, the choice of the contact thickness highly depends on the practical configuration studied.

4.4. *Validation and benchmark*

In order to validate the results of this study it is necessary to proceed into steps. First, the relevance of the results provided by the numerical methods has to be confirmed, and second, if one wants to apply this solution to various real configurations, the effectiveness of the model for those cases has also to be proven. In other words, the assumptions made in Section 2 must be valid and the model must be representative for the specific hydrodynamic contact studied.

Here we will limit the tests to the algorithms examination, the second step being related to experimental tests and future research.

Before moving to the algorithms examination we will introduce some simulation examples. In Figure 10(a), we present an example of simulated asperity, a truncated cone opening, while Figure 10(b) shows a topographic image of a real rough metal surface. Examples of computation results carried out on the topographic image from Figure 10(b), with the NS-r algorithm, are provided as follows. The parameters of the 3D contact are given in Table I.

The v_1 component, the most significant component of the velocity field, is represented in Figure 11. We notice the highest velocity values on $\mathscr{P}$ boundary (10 m/s) and zero values at the interface between $\mathscr{R}$ and the fluid.

4.4.1. Couette flow. A first test to carry out is to check whether the algorithms presented give the expected results for the simplest configuration, that of the planar Couette flow, for

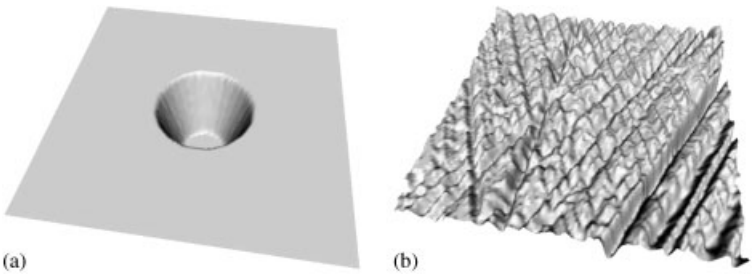

Figure 10. Rough surfaces: (a) Simulated asperity; and (b) topographic image.

Table I. Simulation example—contact parameters.

Parameter	Value	Parameter	Value
v_p	10.0 m/s	l_1	384.0 μm
p_1	20.0 bar	l_2	384.0 μm
p_2	10.0 bar	l_3	3.0 μm
ρ	900.0 kg/m^3	$\triangle x_1$, $\triangle x_2$	3.0 μm/pixel
ν	6.0×10^{-6} m^2/s	$\triangle x_3$	0.1 μm/level

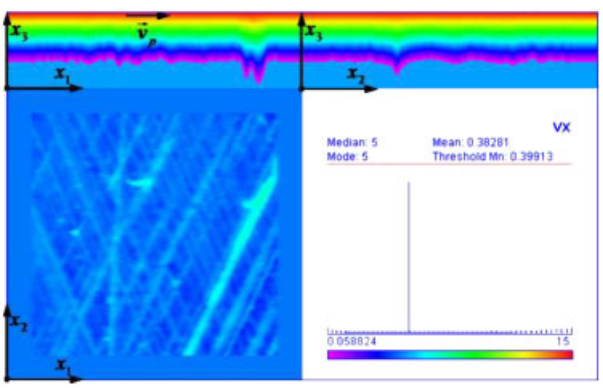

Figure 11. Example of the v_1 velocity field—cuts representation.

which the analytical solution is known (Section 3.2). The contact parameters are those given in Table I.

Figure 12(a) and (b) present a parallel between pressure and v_1 velocity profiles given on the one hand by the analytical results, and on the other hand by the three algorithms chosen in Section 3.4, NS-p, NS-r and RE-r.

In terms of physical measures, a comparison between the three methods via three tribological parameters is provided in Table II. The values estimated by the different methods are very close to those provided by the analytical solution.

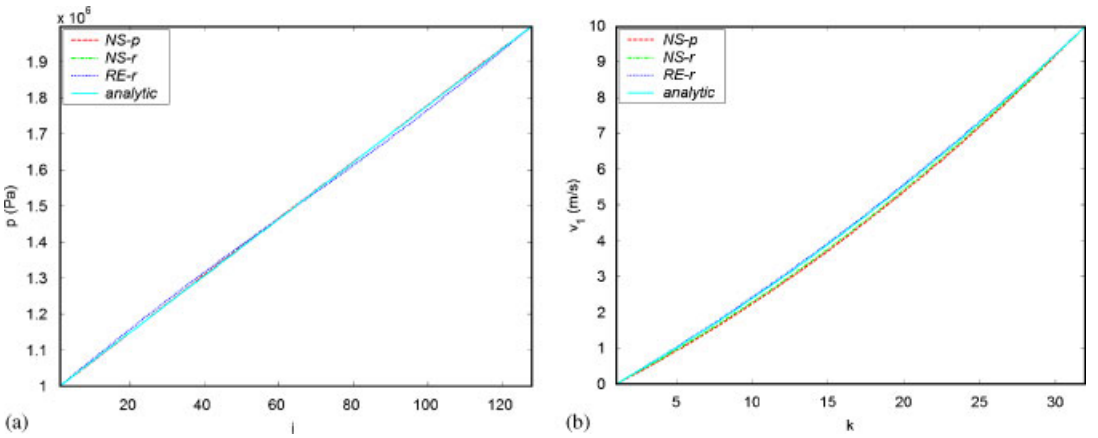

Figure 12. Couette flow—pressure and velocity profiles: (a) p—linear profile; and (b) v_1—parabolic profile.

Table II. Couette flow—measures.

Method	Friction losses (mW/mm^2)	PMF (milibar)	Load (bar)
NS-p	96.946	0.250	15.011
NS-r	96.294	0.243	15.001
RE-r	95.484	0.236	14.995
Analytic	*95.481*	*0.236*	*15.000*

We remind that the Couette flow satisfies the assumptions c_6 and c_7 required by the Reynolds equation. From Table II, we conclude that RE-r provides accurate results, very close to those given by the analytical method. As to NS-p and NS-r, their accuracy is still very good, taking into account their greater computational complexity compared to RE-r, which is largely sufficient for this simple case.

4.4.2. Flow over simple profiles. Another configuration for which the analytical solution may be computed is the flow over simple profiles like the one presented illustrated in Figure 13(a). The 2D contact model is presented in Figure 13(b). The trapezoidal profile is constant on x_2-axis, the contact height varies only with x_1. For this configuration, Navier–Stokes equations would still give a rather complex analytical solution. Instead, we will use Reynolds equation, whose expression is

$$\frac{\partial}{\partial x_1}\left(h^3\frac{\partial p}{\partial x_1}\right) = 6\mu v_p\frac{\partial h}{\partial x_1} \tag{39}$$

Subsequently, the analytical expression of the pressure and velocity fields may be obtain.

Then, we compare this analytical solution with the simulation results for this particular configuration. The contact parameters are given in Table III and no cavitation condition was used. Figure 14(a) and (b) present a comparison between pressure and v_1 velocity profiles

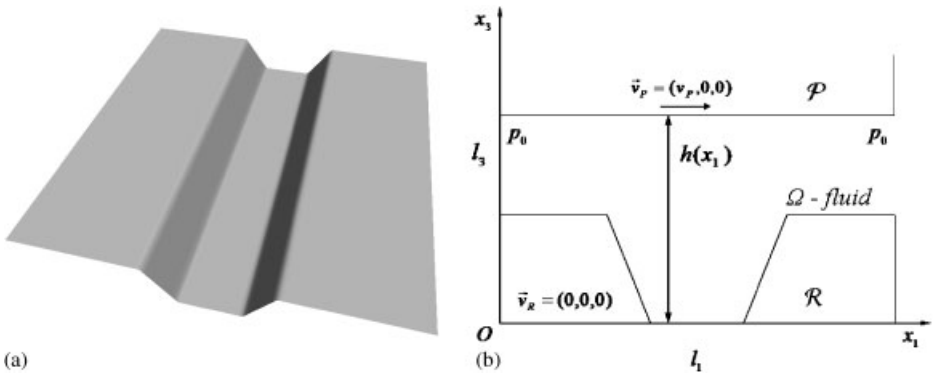

Figure 13. Simple profile configuration: (a) Trapezoidal profile; and (b) 2D contact.

Table III. Flow over simple profiles—contact parameters.

Parameter	Value	Parameter	Value
v_p	10.0 m/s	l_1	384.0 μm
p_1	1.01325 bar	l_2	384.0 μm
p_2	1.01325 bar	l_3	3.0 μm
ρ	900.0 kg/m^3	$\triangle x_1$, $\triangle x_2$	3.0 μm/pixel
ν	6.0×10^{-6} m^2/s	$\triangle x_3$	0.1 μm/level

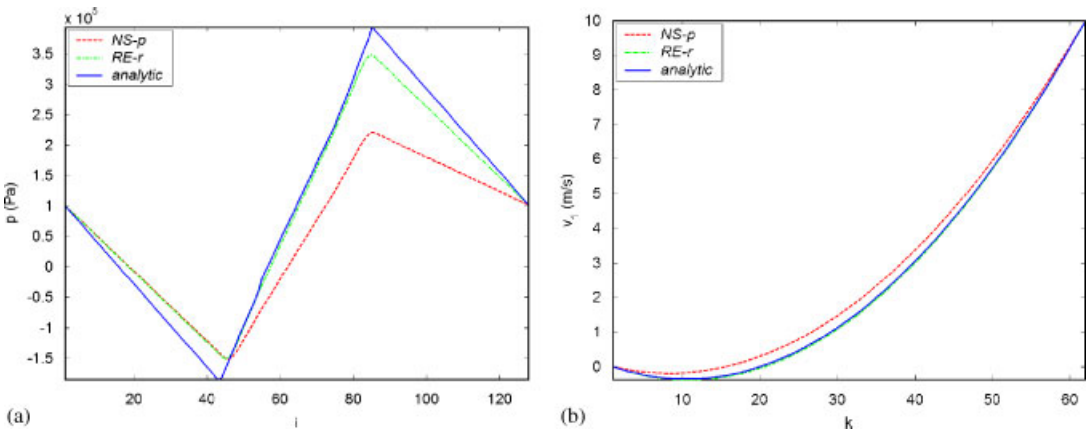

Figure 14. Flow over simple profiles—pressure and velocity: (a) p profile; and (b) v_1 profile.

given on the one hand by the analytical solution, and on the other hand by the NS-p and RE-r numerical methods. NS-r has not been tested as the restrictive boundary conditions do not suit to this particular profile geometry.

We observe good correlation between RE-r and the analytic solution of the Reynolds equation. The results provided by NS-p are slightly different as this method is based on the full Navier–Stokes equations and take into account the inertial terms.

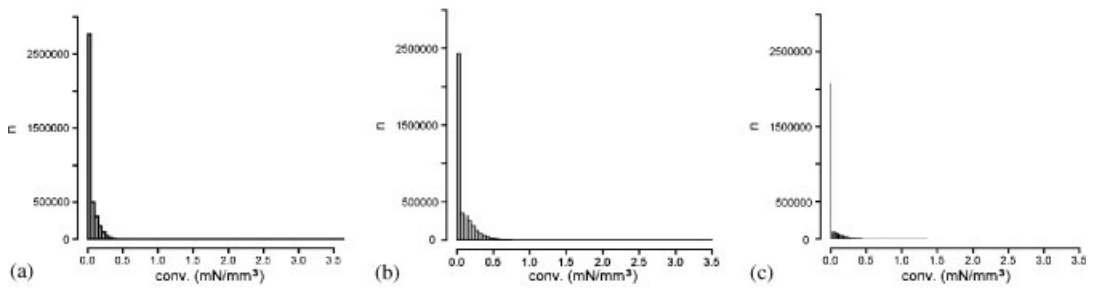

Figure 15. Convective terms—histograms: (a) NS-p; (b) NS-r; and (c) RE-r.

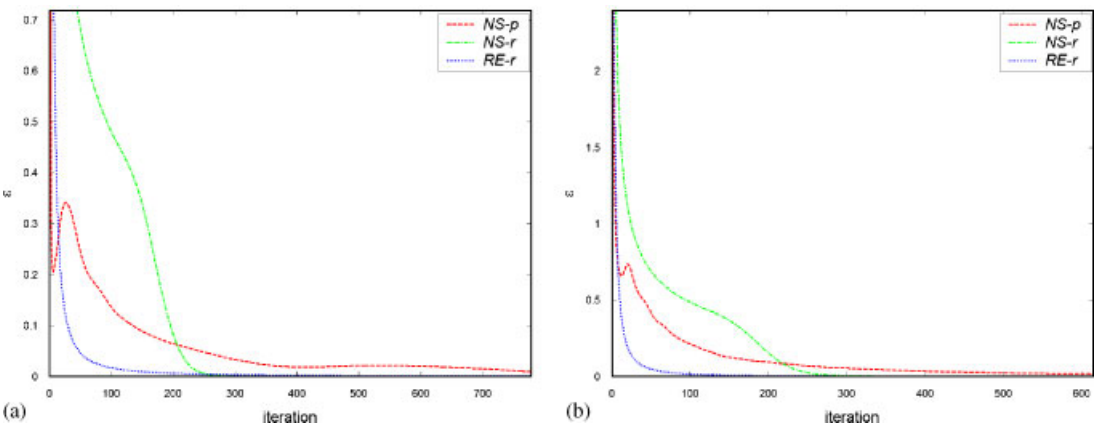

Figure 16. Convergence rate: (a) Simulated asperity; and (b) topographic image.

4.4.3. Non-laminar flow. We will now study the behaviour of the algorithms for contacts containing the rough surface shown in Figure 10, which may involve non-laminar flows. As c_7 is no longer valid, the results provided by RE-r will be examined and compared with those given by the Navier–Stokes solvers. The contact parameters are those given in Table I.

In Figure 15, we plot the histograms of the convective (turbulence) terms $(\boldsymbol{v}\cdot\nabla)\boldsymbol{v}$ computed with the three methods for a contact using the topographic image (Figure 10(b)). We observe that RE-r outputs much smaller convective terms than the other two methods which, contrary to RE-r, take turbulence into account. Indeed, we deal with a rough surface which may not guarantee the laminar flow assumption made by RE-r.

4.4.4. Convergence rate. The convergence rate gives substantial information on the computational time. In the figures above, the global difference between two successive computed (pressure) fields, divided by the number of computation points, is plotted against the iteration step. The stop criterion is satisfied when this difference becomes smaller than the normalized value 0.001. We represent the convergence rate of NS-p, NS-r and RE-r for the simulated roughness contact in Figure 16(a), and for the topographic surface contact in Figure 16(b). A

Table IV. Restrictive boundaries—contact parameters.

Parameter	Value	Parameter	Value
v_p	10.0 m/s	l_1	256.0 μm
p_1	10.0 bar	l_2	256.0 μm
p_2	10.0 bar	l_3	3.0 μm
ρ	900.0 kg/m^3	$\triangle x_1$, $\triangle x_2$	1.0 μm/pixel
v	6.0×10^{-6} m^2/s	$\triangle x_3$	0.1 μm/level

Table V. Restrictive boundaries—measures.

Method	Friction losses (mW/mm^2)	PMF (milibar)	Load (bar)
NS-p	94.937	0.199	9.568
NS-r (10% padding)	94.830	0.195	9.999
NS-r (20% padding)	94.816	0.195	9.999
RE-r	94.814	0.195	9.997

first result emerging from the figures above is the inflection showed by the NS-p algorithm convergence curve. This proves that for the projection method the chosen boundary conditions are essential; an inadequate option could compromise the convergence.

We can notice that among the three methods NS-p is characterized by the longest computation time, having a slow update rate. In return, NS-r starts strongly, making substantial updates, and stops abruptly after few iterations. The important modifications made during the first steps may be responsible for the numerical instabilities discussed in Section 3.2. As for RE-r, it quickly approximates a near-accurate solution and converges rather slowly towards the final solution. However, it should be noticed that if n is the characteristic size of the 3D computation volume, the computation time cost to scan the entire volume is proportional to n^3 for NS-p and NS-r, and to n^2 for RE-r. Thus, RE-r is far more rapid in terms of computation time.

4.4.5. Restrictive boundaries. Another interesting test to perform is to prove the relevance of the boundary solution put forward in Section 3.2. We will check whether the restrictive boundary conditions (implemented with NS-r) lead to the same results as the NS-p and RE-r algorithms. In order to do so, computations on the topographic image (Figure 10(a)) are carried out, using the contact parameters mentioned in Table IV.

The level of the added smooth margins matches $\mathscr{R}$ *median* value and their size represents 10% (respectively 20%) of $\mathscr{R}$ size. Table V presents a parallel, in terms of physical measures, between the different algorithms employed.

We compare in Figure 17 the pressure field output by NS-r (10% padding) with those given by NS-p and RE-r. The maximum differences given by the histograms ($\sim$0.8 bar) are small compared to the pressure inside the contact (10 bar); in addition, the histograms are concentrated at the origin, which proves a good resemblance.

In a similar way, we illustrate in Figure 18 the histograms of the differences between the velocity fields output by the different algorithms. We deal once more with values concentrated

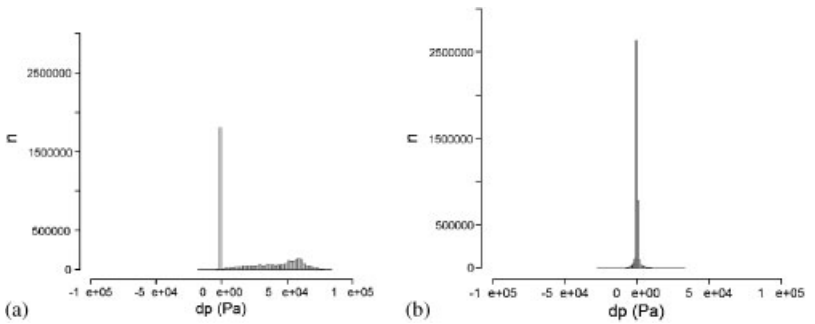

Figure 17. $\triangle p$ histograms: (a) NS-r–NS-p; and (b) NS-r–RE-r.

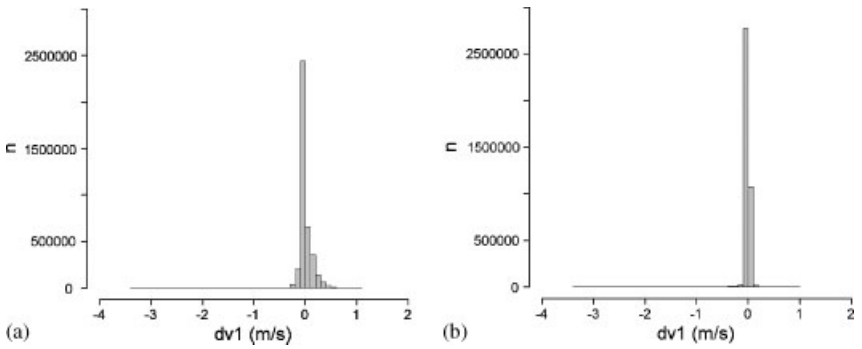

Figure 18. $\triangle v_1$ histograms: (a) NS-r–NS-p; and (b) NS-r–RE-r.

at the origin of the histograms, which proves the small influence of the restrictive boundary conditions on the flow inside the contact.

4.4.6. Resolution and accuracy. For contacts of rough surfaces, the resolution of the input image details is crucial for the computation. We will carry out tests on the surface represented in Figure 10(b) by introducing its associated image into the model with various resolutions, coarser and coarser, multiples of the initial image resolutions. Table I contains the model parameters for the test with the initial resolutions of the input image. The contact thickness will be defined using the median level of the rough surface.

We work with heterogenous grid spacing, $\triangle x_3 = 0.1\,\mu\text{m}$ is very small compared to $\triangle x_1 = \triangle x_2 = 1.0\,\mu\text{m}$. For $L \simeq l_3$, $Re \simeq 10$ and using (17) we deduce the Kolmogorov micro-scale on the x_3-axis, $\eta_3 \sim 0.9\,\mu\text{m}$. Analogously, on the x_1 and x_2 axes, the characteristic length is $L \simeq l_1$ and the associated micro-scale would be $\eta_{1,2} \sim 2.7\,\mu\text{m}$. For accuracy reasons, as mentioned in Section 3.1.1, the grid spacing must not exceed the Kolmogorov micro-scales. Table VI contains the test results for different sampling steps $\triangle x_1$, $\triangle x_2$.

We observe a rather significant gap in the kinetic power dissipation when the grid spacing goes from $2\,\mu\text{m}$ ($< \eta_{1,2}$) to $4\,\mu\text{m}$.

Table VI. Measures—various resolutions.

	Friction losses (mW/mm^2)		
$\triangle x_1$, $\triangle x_2$ (μm)	NS-p	NS-r	RE-r
1	95.519	93.396	92.516
2	95.620	93.627	92.435
4	93.776	91.501	90.010
8	94.124	89.916	87.864

5. CONCLUSION

A model has been developed to investigate the effect of roughness on the fluid flow taking place in a hydrodynamic contact. Well-known DNS methods working with finite differences, based on Reynolds or Navier–Stokes equations, have been adapted and employed; the applicability of these methods to our specific problem has been discussed. A friction prediction tool is in such wise constituted working with rough surfaces represented as 2D input images; this makes it very easy to manipulate for further tests and research.

The model was subjected to a first series of tests to conclude on the relevance of the numerical methods employed and the results are encouraging; the methods show good convergence and accuracy. Furthermore, future work will enable us to verify the effectiveness of the model to simulate real configurations via comparison with experimental tribological tests.

ACKNOWLEDGEMENTS

The research reported here is the result of cooperation between ENSMP (École des Mines de Paris)/ ARMINES, ENSMM (École Nationale Supérieure de Mécanique et de Microtechniques) Besançon, Total, Mecachrome (JPX), PSA (Peugeot-Citroën), Renault and ADEME (Agence de l'Environnement et de la Maîtrise de l'Energie). The partners' support is gratefully acknowledged by the authors.

REFERENCES

1. Decencière E, Jeulin D. Morphological decomposition of the surface topography of an internal combustion engine cylinder to characterize wear. *Wear* 2001; **249**:482–488.
2. Landau L, Lifchitz E. Mécanique des fluides. Ellipses, 1994.
3. Moulinec C, Contribution á la simulation numérique d'écoulements tridimensionnels sur des géométries complexes, Ecole Centrale de Nantes, thése, 1996.
4. Cotoi I. Étude asympthotique de l'écoulement d'un fluide visqueux incompressible entre une plaque lisse et une paroi rugueuse, Univerisité Blaise Pascal, thése, 2000.
5. Sanda S, Someya T. The effect of surface roughness on lubrication between a piston ring and a cylinder liner. *Proceedings of the Institution of Mechanical Engineers* 1987; **1**(C223):135–143.
6. Ronen A, Etsion I, Kligerman Y. Friction-reducing surface-texturing in reciprocating automotive components. *Tribology Transactions* 2001; **44**:359–366.
7. Peyret R, Taylor TD. *Computational Methods for Fluid Flow*. Springer: Berlin, 1990.
8. Quartapelle L. *Numerical Solution of the Incompressible Navier–Stokes Equations*. Birkhauser: Basel, 1993.
9. Hamilton DB, Halowit JA, Allen CM. A theory of lubrication by micro-irregularities. *Journal Basic Engineering* 1966.
10. Priest M, Dowson D, Taylor CM. Theoretical modelling of cavitation in piston ring lubrication. *Proceedings of the Institution of Mechanical Engineers*, *Part C-Mechanical Engineering Science* 2000; **214**:435–447.
11. Turek S. Efficient solvers for incompressible flow problems: an algorithmic approach in view of computational aspects, Universität Heidelberg, 1998.

12. Ferziger JH, Peric M. *Computational Methods for Fluid Dynamics* (3rd edn). Springer: Berlin, 2002.
13. Vuik C, Wesseling P, Zeng S. *Krylov Subspace and Multigrid Methods Applied to the Incompressible Navier–Stokes Equations*. Faculty of Technical Mathematics and Informatics, TU Delft Netherlands, 1995.
14. Ciarlet PG. Introduction à l'analyse numérique matricielle et á l'optimisation, Dunod, 1990.
15. Quarteroni A, Saleri F, Veneziani A. Factorization methods for the numerical approximation of Navier–Stokes equations. *Computer Methods in Applied Mechanics and Engineering* 2000; **188**:505–526.
16. Brown D, Cortez R, Minion M. Accurate projection methods for the incompressible Navier–Stokes equations. *Journal of Computational Physics* 2001; **168**:464–499.

